Bioinspired Fiber Networks with Tunable Mechanical Properties by Additive Manufacturing

Mainak Sarkar, Jacob Notbohm

Department of Mechanical Engineering
Department of Engineering Physics
University of Wisconsin–Madison
Madison, WI, USA

Keywords

Fiber Network, Computational Geometry, Mesh Generation, 3D Printing, Additive Manufacturing, Bioinspired Materials

Abstract

Soft bioinspired fiber networks offer great potential in biomedical engineering and material design due to their adjustable mechanical behaviors. However, existing strategies to integrate modeling and manufacturing of bioinspired networks do not consider the intrinsic microstructural disorder of biopolymer networks, which limits the ability to tune their mechanical properties. To fill in this gap, we developed a method to generate computer models of aperiodic fiber networks mimicking type I collagen ready to be submitted for additive manufacturing. The models of fiber networks were created in a scripting language wherein key geometric features like connectivity, fiber length, and fiber cross section could be easily tuned to achieve desired mechanical behavior, namely pretension induced shear stiffening. The stiffening was first predicted using finite element software, and then a representative network was fabricated using a commercial 3D printer based on digital light processing technology using a soft resin. The stiffening response of the fabricated network was verified experimentally on a novel test device capable of testing the shear stiffness of the specimen under varying levels of uniaxial pretension. The resulting data demonstrated clear pretension-induced stiffening in shear in the fabricated network, with uniaxial pretension of 40% resulting in a factor of 2.65 increase in the small strain shear stiffness. The strategy described in this manuscript addresses current challenges in modeling bioinspired fiber networks and can be readily integrated with advances in fabrication technology to fabricate materials truly replicating the mechanical response of biopolymer networks.

Introduction

Nature has provided perpetual inspiration in generating advanced materials of impressive mechanical functionalities [1]. Among the several fascinating structural materials nature offers, soft fiber networks with random microstructures are abundant in living systems, as they form the primary load bearing framework of the cellular cytoskeleton [2, 3, 4], the extracellular matrix [5], and blood clots [6]. These networks are comprised of slender fibers that are soft in bending. When subjected to small to intermediate deformations, the fibers primarily bend [7, 8, 9] and realign along the direction of maximal principal stress [10, 11, 12, 13], causing strain stiffening of the fiber network [14, 15, 16, 17, 18, 19]. Interestingly, a residual stress or pre-stress in the form of uniaxial tension, commonly observed in biopolymer networks [20, 21, 22, 23], stiffens them in shear as well [8, 24, 25, 26], indicating the existence of a complex coupling between tension and shear in these materials. This unique characteristic of strain-induced stiffening makes these networks mechanically adaptive to environmental complexities [27, 28], and some attempts were made in mimicking these intricate mechanics with soft synthetic materials [29, 30]. The potential use of such bioinspired networks are diverse, for example, in the development of artificial tissue constructs due to the tunability of their mechanical properties to match the properties of organs [29, 31] and in the design of flexible electronic and energy devices owing to their adjustable stretchability [32, 33, 34].

Light-based additive manufacturing technologies, such as selective laser sintering [35] and digital projection lithography [36], provide ample opportunities to fabricate soft bioinspired networks with highly complex micro-architectures. Although these technologies have been used to fabricate synthetic scaffolds for myocardial tissue [37], cartilage [38], and liver lobule [39], the prior studies were restricted to fabrication of lattice-based models, wherein the structure was spatially periodic. The networks were able to precisely match the number of fibers and connections to the biopolymer networks, but they lacked the intrinsic morphological disorder that biopolymer networks possess. This disorder is useful to achieve desired global mechanics in fabricated networks; for example, tuning the degree of disorder changes the critical strain for strain stiffening [40]. Unlike lattice structures, aperiodic network models cannot be created expediently on the graphical user interface of conventional computer-aided design (CAD) software [41]. Additionally, most of the existing methods to fabricate random fiber networks, such as chemical vapor deposition [42], electrospinning [43], and drop-casting [44] do not replicate a computer model implying limited control over the network architecture. Addressing these challenges is a starting point in truly emulating the intricate geometry and thereby the mechanics of biopolymer networks.

Here, we filled this gap by developing a method to additively manufacture fiber networks from computational models that resembled the structure of type I collagen gels. The models were developed in a scripting environment, meaning that morphological features like the connectivity (*i.e.*, the number of of fibers joining at each node), fiber length, and fiber cross section were readily tunable. The numerical model enabled mechanics-based modeling by treating the fibers as beams in finite element software (similarly to refs. [45, 26]), which was used to quantify the small strain shear stiffness under for varying levels of uniaxial tensile prestress. We also manufactured a representative fiber network using a commercial three-dimensional (3D) printer, and we built a novel test device to verify that the printed specimen exhibited tension-induced stiffening in shear, similar to both the finite element predictions and to networks made of collagen fibers. The experimental results from the tests on the 3D printed specimen were then compared with the results of the finite element simulation.

Methods

We developed a workflow to fabricate computer models of fiber networks and developed a test device to demonstrate a strain-induced stiffening in a representative 3D printed network. Below, we elaborate on each step.

Generation of Computer Model of the Fiber Network

We created a two-dimensional (2D) model inspired by the structure of type I collagen. Although collagen matrices are 3D, their strain stiffening behavior wherein their tangent modulus depends on applied stress is exactly preserved in 2D network models [7]. We generated Voronoi networks following refs. [46, 47] and introduced further disorder by performing a random deletion of a few fibers, similar to ref. [26]. In brief, random seeds were scattered within a 2D domain to generate a Voronoi tessellation, with the edges of the resulting polygons being the fibers. The random fiber network thus generated was subjected to further disorder by arbitrarily removing 3% of the total number of fibers from its domain (Fig. 1a). As expected from the literature [48], the fiber lengths in this Voronoi-based network were Poisson-distributed, and they were fully characterized by the average fiber length (L_f), which in the present case was 3.9 mm. In view of the fact that collagen networks exhibit average nodal connectivity well below the Maxwell's isostatic threshold of $2d$ (with d being the system dimension) [49], the diluted 2D Voronoi networks had an average connectivity of 2.8, which was less than the Maxwell's 2D isostatic threshold of 4.

Network models like this one, having randomness and tunability in fiber length, alignment, and connectivity, are not feasible to develop using commercial CAD software, because such software is restricted to periodic lattice-based models, as in prior studies [37, 38, 39]. Here, rather than using CAD software, we created the line diagram of the disordered fiber network (Fig. 1a) in a scripting language. Our steps to convert the line diagram into a fabricable model are described below, and our software is freely available at the link given in the Code Availability Statement.

Modeling the Fibers

Individual fibers were modeled as three-dimensional beams of rectangular cross section having width $w = 0.5$ mm in the x–y plane and height $h = 1.5$ mm in the z direction. The susceptibility to fiber bending is commonly measured by the ratio of the fiber's bending stiffness to stretching stiffness, which we refer to as the dimensionless bending stiffness, $\kappa = EI/EAL_f^2$, where E, A, and I are the Young's modulus, cross sectional area, and moment of inertia of each fiber [50, 51, 52, 53]. Here, for the rectangular cross section, $\kappa = w^2/12L_f^2 = 1.4 \times 10^{-3}$, which is a typical value for fibers in networks of type I collagen and fibrin [7, 54, 24].

We used Standard Tessellation Language (STL) to create the geometry of each fiber as an isolated three-dimensional triangular mesh meaning that the surface contours of each fiber were defined by a series of connected triangles. The meshes defining each fiber were subsequently placed along the edges of the polygons in the Voronoi network (Fig. 1b,c). Finally, the meshes were combined and exported as a single file that contained one object of disconnected fiber meshes that overlapped one another near the nodes of the network (Fig. 1c).

Boolean Union of Fiber Meshes

The file from the previous step was imported to the commercial CAD software Netfabb (Autodesk) to perform an union of the volumes of the disconnected fiber meshes (Fig. 1c and Fig. 2a) at the regions of their overlap. Firstly, the surfaces of the fiber meshes inside the unified volume of the network were removed. Then the triangles of the disjoint meshes were stitched through re-triangulation to generate a watertight, continuous mesh representing the entire network (Fig. 2b). Each edge in this final mesh was shared exactly by two neighboring triangles. The mesh triangles were unique, not self-intersecting, and their normals were always oriented away from the volume enclosed by the mesh. The final mesh, encoded in STL, was ready to be exported to a commercial slicing software specific to the 3D printer's manufacturer. The necessary scripts and the workflow to generate models of fiber networks and export the STL files for additive manufacturing are available in a public repository at the link given in the Code Availability Statement.

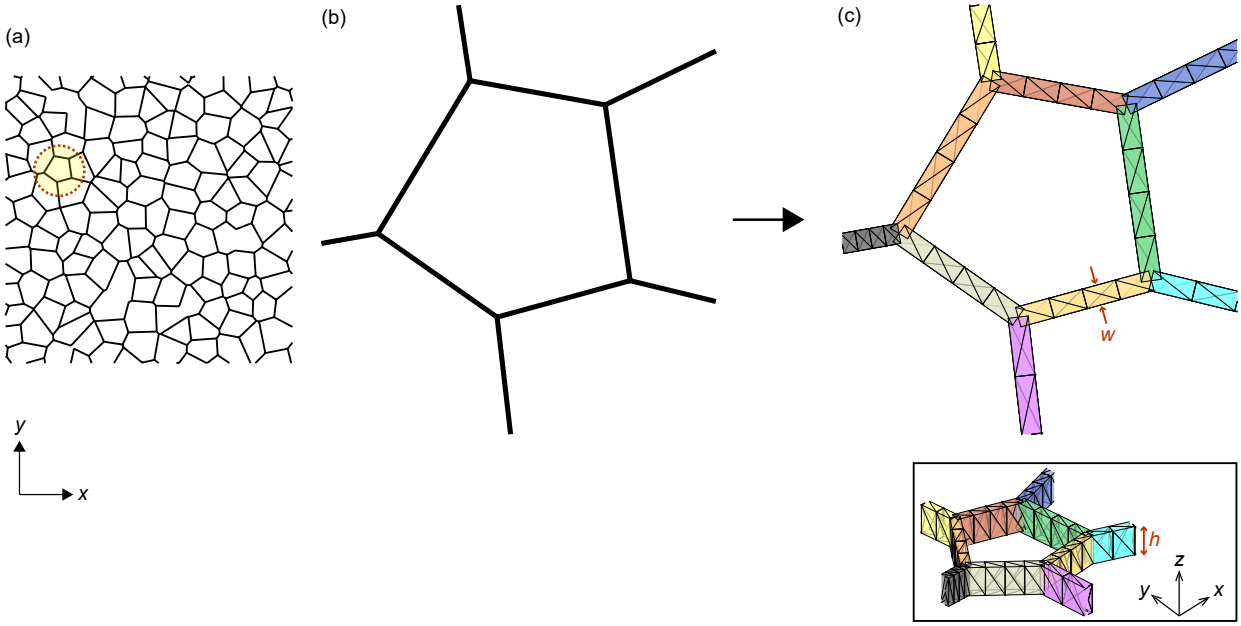

Figure 1: Architecting the computational model of fiber network. (a) A portion of the diluted Voronoi network of randomly organized fibers. A representative polygon is highlighted in yellow. (b) An enlarged version of the representative polygon from panel a. (c) Plan view of the representative polygon of panel b when the isolated meshes of three-dimensional fiber beams with rectangular cross section ($w \times h$) were placed along its edges. The inset shows the corresponding isometric view.

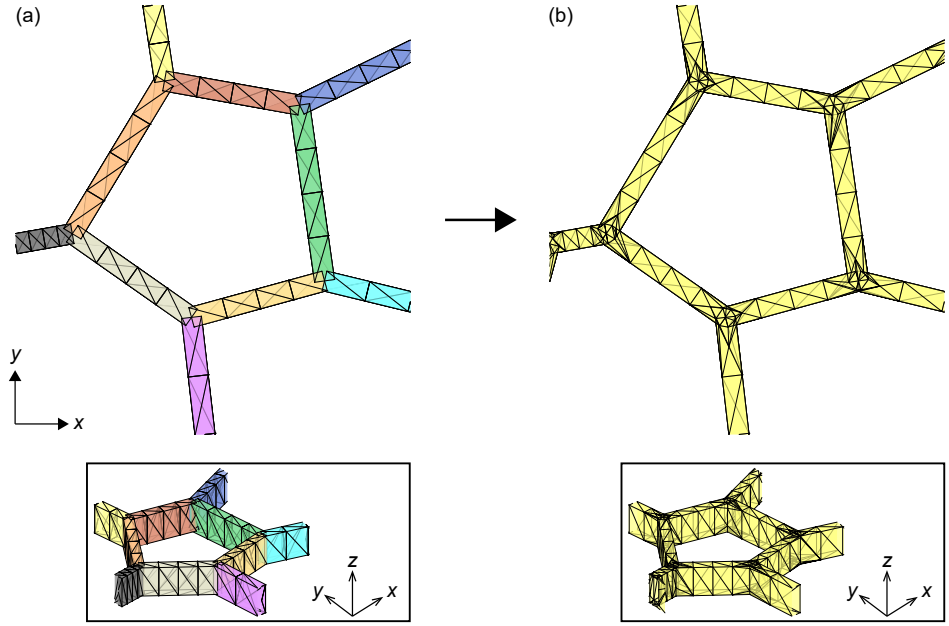

Figure 2: Boolean union of fiber meshes. (a) Plan and isometric (inset) view of the representative polygon considered in Fig. 1 with the mutually disjoint meshes of fibers along its edges. (b) Isolated fiber meshes in panel a were merged at the locations of their mutual overlap to form a watertight continuous mesh. Inset shows the isometric view of the merged mesh.

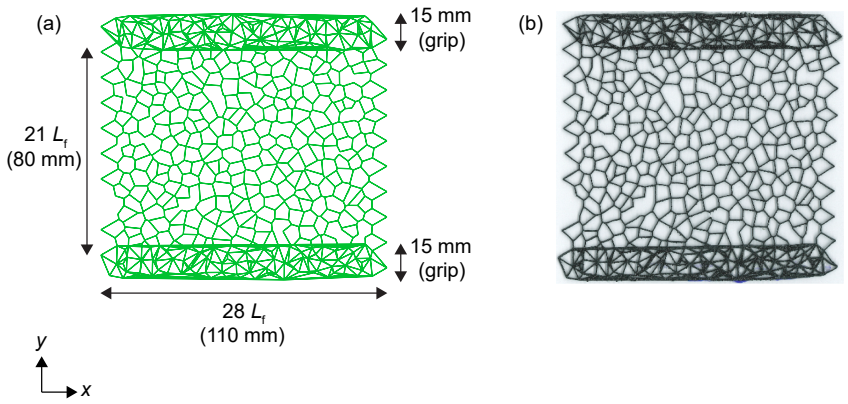

Figure 3: Fabrication of the fiber network model. (a) The STL model of the fiber network submitted for fabrication. It had overall in-plane (x–y) design dimensions 110 mm × 110 mm and out-of-plane (z) thickness 1.5 mm. The average fiber length (L_f) was 3.9 mm. The 15 mm thin strips at the top and bottom of the network were densified to facilitate gripping the printed specimen on the test frame during mechanical testing. (b) Photograph of the manufactured (3D printed) model of the network.

Slicing the Network Mesh

The STL file of the model was processed in a slicing procedure to generate a text file, called G-code, with commands to run a 3D printer for printing the model network. This procedure analysed the model layer by layer to add to it the necessary mechanical supports during the printing process, which later were manually removed from the finished printed part.

Selection of Fabrication Technology and Material

The network was printed by a commercial 3D printing service provider (Midwest Prototyping, Blue Mounds, WI) using an M2 3D printer (Carbon Inc.), which is based on Digital Light Processing (DLP) technology. In brief, the DLP method rapidly fabricates a 3D object layer by layer through spatially controlled solidification of a photo-curable resin [55, 56]. Due to high achievable in-plane resolution as low as 75 µm and out-of-plane resolution $\leq$ 100 µm, this method is suitable for printing complex lattices as demonstrated by prior studies [57, 58]. Our goal was to fabricate a soft network (similar to ref. [59]) with fibers undergoing bending-dominated deformation under loading, and therefore the resin chosen was a shore A polyurethane elastomer, EPU 40 (Carbon Inc.), with hardness 68 durometer as reported by the manufacturer. The values of Young's modulus and Poisson's ratio of EPU 40 have been reported to be 6.81 MPa and 0.48, respectively [60].

Specimen Dimensions

The in-plane (x–y) dimensions of the print bed of an M2 3D printer, 189 mm × 118 mm, constrained the design dimensions of the model network to be printed. We chose to print a square model having overall in-plane dimensions 110 mm × 110 mm and out-of-plane thickness 1.5 mm (Fig. 3a). The densified regions at the top and bottom of the network (labeled "grip" in Fig. 3a) facilitated gripping the printed specimen (Fig. 3b) on the test frame during the mechanical testing described in the section "Experimental Device to Mechanically Test the Printed Specimen."

Finite Element Simulations with the Numerical Model

We applied simple shear combined with uniaxial prestress on the numerical model of the network by performing 2D finite element simulations using the commercially available finite element software Abaqus

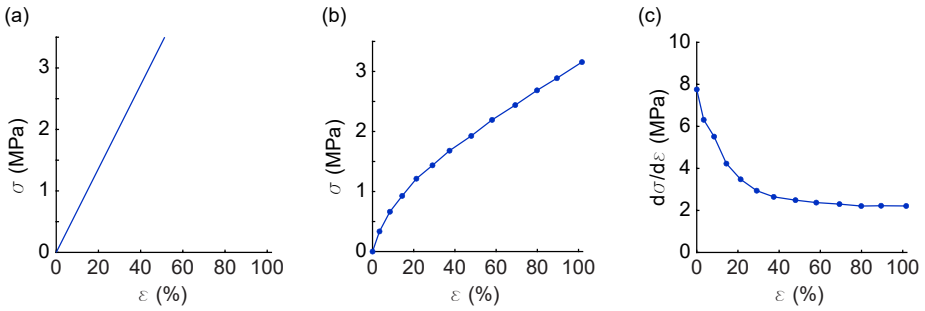

Figure 4: Constitutive material models of the fibers used in the simulations. (a) A linear tensile stress–strain response (σ–ε), with Young's modulus 6.81 MPa. (b) The nonlinear tensile stress–strain response (σ–ε) of the printing resin (EPU 40), digitized from the graph published by the manufacturer (Carbon). (c) The evolution of tangent modulus ($d\sigma/d\varepsilon$) of EPU 40 with respect to the applied tensile strain (ε). This plot depicts considerable strain softening of EPU 40.

(Dassault Systèmes). Fibers of rectangular cross section (0.5 mm $\times$ 1.5 mm) were modeled as elastic and isotropic beams using two three-noded quadratic beam elements, following earlier studies [61, 51, 62, 63, 64]. Some simulations considered simplified linear material response for the fibers (Fig. 4a), with the value of Young's modulus $E = 6.81$ MPa, as reported previously for EPU 40 [60]. Another set of simulations considered the fibers to possess a nonlinear material stress-strain curve, acquired by digitizing the manufacturer's published stress–strain curve for EPU 40 (Fig. 4b). In all simulations, the Poisson's ratio (ν) of the fibers was set to 0.48, as reported previously [60]. The connections between fibers were "welded" meaning they transmitted both forces and moments. We evaluated the response of the network using two different solvers as described in the following sections. The global stress and strain measures used in the simulations were the engineering stress and strain.

Implicit Dynamic Quasi-Static Solver

For instances where the fibers were modeled as linear elastic beams (Fig. 4a), the implicit dynamic quasi-static solver with the option of nonlinear geometry was used for the computations, as in our prior work [65, 66, 64]. Since the system contained severe geometric nonlinearities, we applied the displacement boundary condition in small load steps (0.05% global strain per step) to ensure that the solver converged to static equilibrium with practically negligible convergence bias. We subjected the network to several levels of uniaxial pretension, $\varepsilon = 0,\ 10,\ 20,\ 30,\ 40\%$ and small simple shear up to $\gamma = 3\%$. In terms of the computation time, this solver was $\approx 5\times$ faster than the explicit dynamic solver described in the next section.

Explicit Dynamic Solver

The tensile stress-strain response of the printing resin (EPU 40) is nonlinear (Fig. 4b) and depicts strain-softening (Fig. 4c). We introduced this material nonlinearity in our model of the network by considering fibers to possess nonlinear tensile response, exactly matching that of EPU 40 (Fig. 4b). The implicit solver described above was unable to converge when using the nonlinear material model, so we used the Abaqus explicit dynamic solver with the nonlinear geometry option, following our earlier study [13]. Sufficient damping and an optimum time of analysis were considered to attain a quasi-static, steady state at each increment in displacement. Since convergence of the solver can be erroneous if the model is overdampled, we tuned the damping coefficient to ensure that the model was slightly underdamped, meaning that the quasi-static steady state was reached when the model's kinetic energy reached a steady state after undergoing a few oscillations. The network was again subjected to several levels of uniaxial pretension, $\varepsilon = 0,\ 10,\ 20,\ 30,\ 40\%$ and small simple shear up to $\gamma = 3\%$. At the point of convergence, the model's steady state kinetic energy always remained less than 0.001% of its strain energy. See Appendix A for more details about how convergence of the explicit solver was verified.

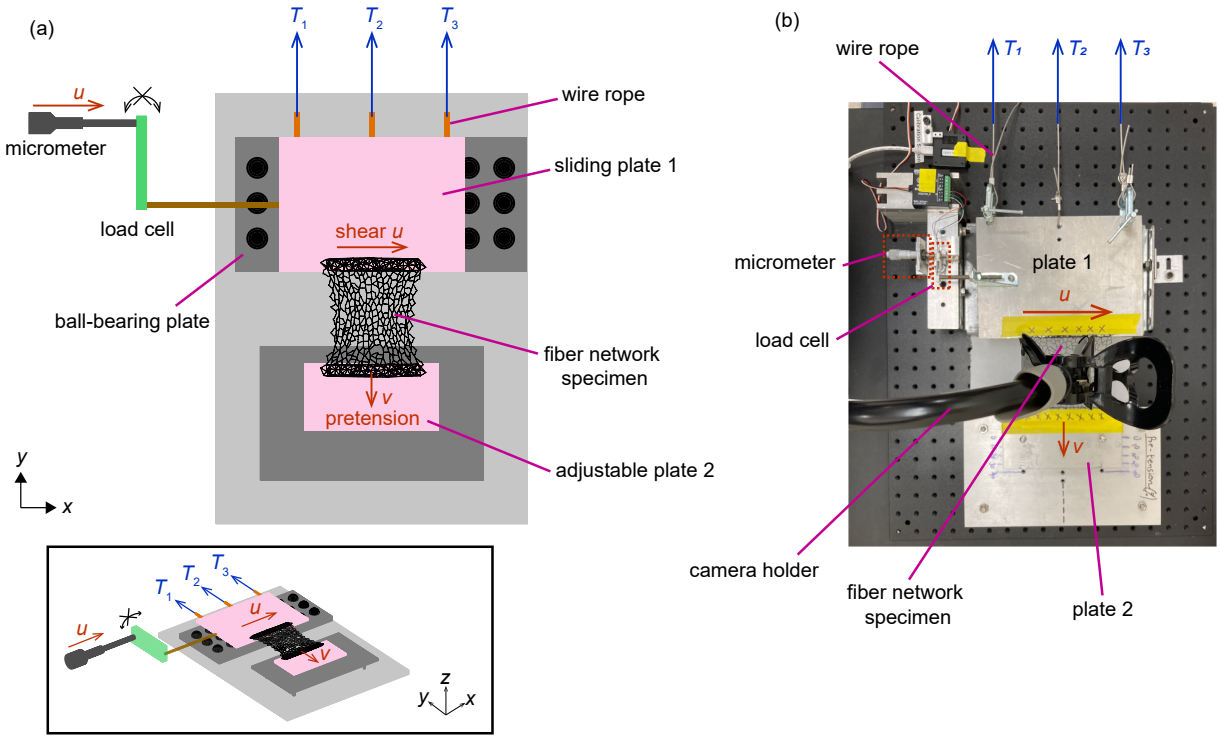

Figure 5: Experimental device to perform mechanical test on the fabricated thin film fiber network specimen. (a) The plan view of the conceptual diagram of the test device. The inset shows the isometric view. (b) The plan view of the real test device.

Experimental Device to Mechanically Test the Printed Specimen

The influence of uniaxial pretension on the small-strain shear stiffness of fiber networks is well established [8, 24, 26, 64] and is one of the key factors used to assess how well the bioinspired printed network reproduces the desired mechanical response. Here, we developed an in-plane test device to apply uniaxial pretension and simple shear on the printed network (Fig. 5a,b).

The existing in-plane shear testing protocol for a thin specimen, ASTM D 7078 [67, 68], cannot induce uniaxial pretension on the specimen necessitating the need for a customized test device. The device, shown conceptually in Fig. 5a, consisted of two quarter-inch thick aluminum plates (labeled "plate 1" and "plate 2") to which the edges of the printed specimen were glued using a cyanoacrylate adhesive (Loctite 401). The dense grip edges of the specimen (Fig. 3b and Fig. 5a) increased the contact area between the glued surfaces and the metal plates and, hence, practically eliminated slip during loading. The use of grips that fix the displacements along with a square specimen can produce a boundary effect, which is common in fiber networks [61, 63, 69]. We considered reducing the boundary effect by increasing the spacing between plate 1 and plate 2 to use a specimen with an aspect ratio larger than unity. To this end, we simulated specimens having varying aspect ratios, but the results showed that even an aspect ratio of 6 would have a substantial boundary effect, meaning the boundary effect could not be eliminated for any dimensions that would be feasible to print (Appendix B). For this reason, we chose to use a square network for the remainder of our study.

The y position of plate 2 was adjusted before testing to induce a desired level of uniaxial pretension in the specimen. At a given pretension, the device fully constrained the movement of plate 2 and allowed the plate 1 to slide on a well-lubricated ball bearing plate in the positive x direction. The translation of plate 1 along y was restricted by the tension produced in three long (≈ 2 m) wire ropes connected to it. All the three

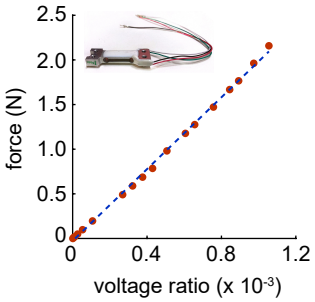

Figure 6: Calibration curve for the load cell. Known calibration weights were plotted against the corresponding voltage ratios recorded by the load cell during calibration. The dashed blue line is the best-fit calibration curve which is linear up to a force of 2.2 N. Inset shows the photograph of the load cell.

wire ropes carried equal tension forces ($T_1 = T_2 = T_3$) when the specimen was under only pretension. Shear deformation was induced by displacing plate 1 in the positive x direction using a micrometer (Mitutoyo, spindle pitch 0.5 mm) connected to the plate through a load cell (Phidgets Inc., 0 to 100 grams). Given that our objective was to quantify the linear shear stiffness in response to different uniaxial pretensions, the range of shear strain applied was 0 to $\approx 5\%$. If a larger shear strain were desired, the only changes to our test device that would be required would be to use a different micrometer and load cell. Shearing tended to cause rotation of plate 1, but the long wire ropes attached to plate 1 remained nearly parallel to the y axis and supported unequal tension forces, $T_1 \neq T_2 \neq T_3$, to restrict its rotation and maintain static equilibrium. A photograph of the test device is shown in Fig. 5b.

Calibration of the load cell was necessary before testing. By construction, this load cell was a cantilever beam with four strain gauges attached to it in a Wheatstone bridge arrangement. At a given applied shear displacement on the specimen, the live end of this cantilever beam deflected causing the electrical resistance of the strain gauges to change, unbalancing the Wheatstone bridge. This circuit was energized with an input voltage, and the ratio of output to input voltage was read by a high resolution analog-to-digital converter (Wheatstone Bridge Phidget, Phidgets Inc.) and recorded by a Python script through the use of the *Phidget22* software library available on the manufacturer's website. To calibrate the load cell, we used several combinations of standard calibration weights. The fitted calibration curve relating the force and the voltage ratio was linear up to a force of 2.2 N (Fig. 6) meaning that this load cell performed linearly even at loads $2.24\times$ the maximum prescribed capacity of 100 grams. We used this calibration curve for the tests on the fabricated specimen.

Results and Discussion

Simulations with the Numerical Model

To verify that the fiber network exhibited pretension-induced shear stiffening, we began with the simplified finite element model of the fiber network considering the linear, elastic constitutive model for the fibers (Fig. 4a). For this simplified model, we used the implicit dynamic quasi-static solver for its robust convergence and computational efficiency, as discussed in the Methods section. We induced uniaxial pretension followed by simple shear on the network. The boundary conditions were applied on the subset of nodes at the top and bottom grips of the network (highlighted blue in Fig. 7a). The nodes in the bottom subset were fixed, and the nodes in the top subset were translated in the positive y direction during pretension (ε). Subsequently, considering the prestrained configuration as the starting point, simple shear (γ) was applied by translating the nodes in the top subset in the positive x direction (Fig. 7a). A representative deformed configuration, corresponding to pretension $\varepsilon = 30\%$ and shear $\gamma = 3\%$, is depicted in Fig. 7b with the

fibers colored by the magnitude of displacement, $|U|$. We determined the stress–strain (τ–γ) responses in small shear (up to $\gamma = 3\%$) at different levels of pretensions $\varepsilon = 0$, 10, 20, 30 and 40% (Fig. 7c). These curves were all linear and the slopes, *i.e.*, the values of small strain shear stiffness G_0, increased with the increasing pretension. G_0 increased by a factor of 12.1 starting from the value of 82.2 kPa at zero pretension ($\varepsilon = 0\%$) to 998 kPa at the highest pretension ($\varepsilon = 40\%$). These observations were similar to observations of prior studies [8, 24, 26, 64], and they confirmed the occurrence of pretension-induced shear stiffening in the network.

Significant axial tensile strains were present in the fibers at large pretensions of the network. For example, the average axial strains experienced by the fibers were $\approx 16\%$ and $\approx 23\%$ at pretensions (ε) of 30% and 40%, respectively (Fig. 7d, e). The resin used to print the specimen (EPU 40) softens at these high levels of strain (Fig. 4c), meaning the use of a linear material model for the fibers could cause errors in predictions of the pretension-induced shear stiffening in the specimen. Therefore, we updated the model by matching the nonlinear tensile response of the fibers to that of EPU 40 (Fig. 4b), and used the explicit dynamic solver as described in the Methods section. We verified that the explicit solver converged correctly (Appendix A) and repeated the simulations of Fig. 7c. We again obtained the stress–strain responses in small shear (up to $\gamma = 3\%$) at all pretensions $\varepsilon = 0$, 10, 20, 30 and 40% (Fig. 7f). The data were linear, and the slopes increased with increasing pretension, but by a smaller factor of 2.64 starting from the value of 82.2 kPa at zero pretension ($\varepsilon = 0\%$) to 216 kPa at the highest pretension ($\varepsilon = 40\%$). A comparison of the results in Figs. 7c and 7f indicates that strain softening in the fibers suppressed the level of pretension-induced shear stiffening in the network, but did not eliminate it.

Mechanical Tests on the Printed Specimen

With the simulations predicting a stiffening response in the finite element model, our next step was to ascertain how well the fabricated model inherited this mechanical behavior. We began with the simplest situation, with no applied pretension, by positioning plate 2 in the test device so as to subject the specimen to no pretension. The specimen was gradually loaded in simple shear by displacing plate 1 along the positive x direction. Due to compliance of the test frame and load cell, the actual shear displacement undergone by the specimen was smaller than that applied to plate 1. Given that reliable quantification of the compliance of the test frame and the load cell was challenging, specimen displacements were measured independently. To this end, the test was videographed to obtain sequential digital images of the specimen (*e.g.*, Fig. 8a). We tracked the images of the moving grip of the specimen (top red box in Fig. 8a) and the displacement of its centroid along x, in pixels, was converted to the physical unit of displacement (mm) to get the applied shear displacement u on the specimen. The shear forces (f) recorded by the load cell were plotted against the corresponding shear displacements (u) and the best-fit response was linear (Fig. 8b).

We repeated this simple shear test by subjecting the specimen to a nonzero pretension $\varepsilon = 10\%$ by adjusting the position of plate 2 in the test device before applying shear. Subsequently, this procedure was repeated for additional different levels of pretension $\varepsilon = 20$, 30 and 40%. One representative image of the specimen is shown in Fig. 9a, where the specimen was subjected to a pretension $\varepsilon = 30\%$ and shear $\gamma = 3.6\%$. The best-fit force–displacement and the engineering stress–strain responses in small shear were all linear (Fig. 9b). The slopes of these curves, that is, the values of small strain shear stiffness (G_0) of the network increased with the increasing pretension. With the range of pretension tested, G_0 increased by $2.65\times$ starting from the value of 77.0 kPa at zero pretension ($\varepsilon = 0\%$) to 204 kPa at the highest applied pretension ($\varepsilon = 40\%$). These observations confirmed a strain-induced stiffening in the fabricated network.

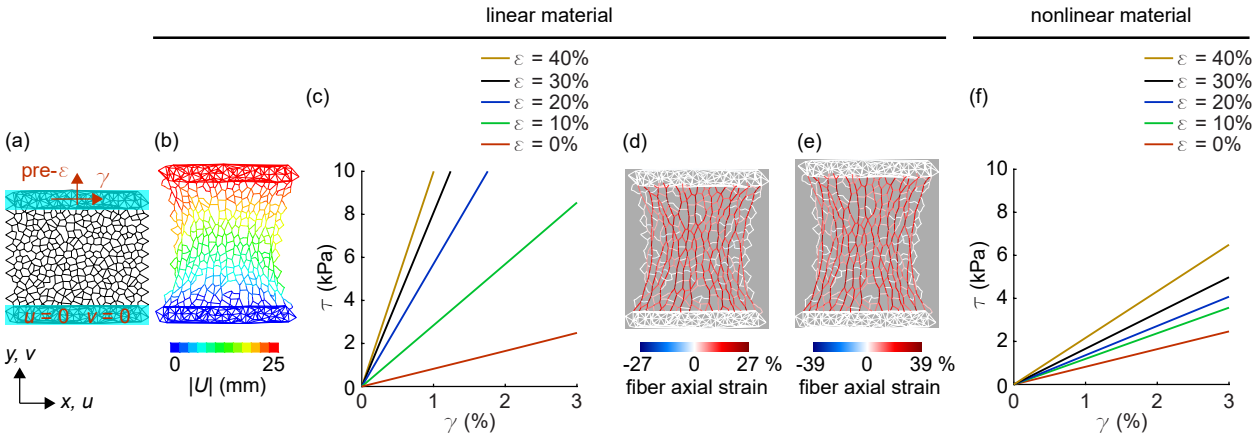

Figure 7: Finite element simulations. (a) After tensile prestrain, the network was subjected to shear strain. The nodes at the bottom of the network were fixed, and the nodes at the top of the network were subjected to uniaxial pretension (ε) followed by shear (γ). (b) Representative deformed state of the network subjected to a prestrain $\varepsilon = 30\%$ and shear strain $\gamma = 3\%$. The fibers in the deformed network are color coded by the magnitude of their displacement, $|U|$. (c) The stress–strain (τ–γ) responses in small shear at different levels of pretension ε in the network. The values of small strain shear stiffness (G_0) as indicated by the slopes of the linear τ–γ responses were 82.2, 284, 570, 808 and 998 kPa for, respectively, pretensions of $\varepsilon = 0$, 10, 20, 30, and 40%. This observed increase in shear stiffness with increasing pretension indicates prestrain-induced stiffening in the modeled network. (d) Representative deformed state of the network subjected to a prestrain $\varepsilon = 30\%$ and shear strain $\gamma = 3\%$. The fibers in the deformed network are color coded by their axial strain. The average axial strain in the fibers was $\approx 16\%$. The range of axial strain in the fibers was $[-2.3, 27]\%$. (e) Representative deformed state of the network subjected to a prestrain $\varepsilon = 40\%$ and shear strain $\gamma = 3\%$. The fibers in the deformed network are color coded by their axial strain. The average axial strain in the fibers was $\approx 23\%$. The range of axial strain in the fibers was $[-3.3, 39]\%$. In panels b–e, the simulations considered the linear material model (Fig. 4a) for the fibers. (f) Simulations considering the nonlinear material model (Fig. 4b) for the fibers. The stress–strain (τ–γ) responses in small shear at different levels of pretension ε in the network are plotted. The values of small strain shear stiffness (G_0) as indicated by the slopes of the linear τ–γ responses were 82.2, 119, 136, 166 and 216 kPa for, respectively, pretensions of $\varepsilon = 0$, 10, 20, 30, and 40%. This observed increase in shear stiffness with increasing pretension indicates prestrain-induced stiffening in the modeled network.

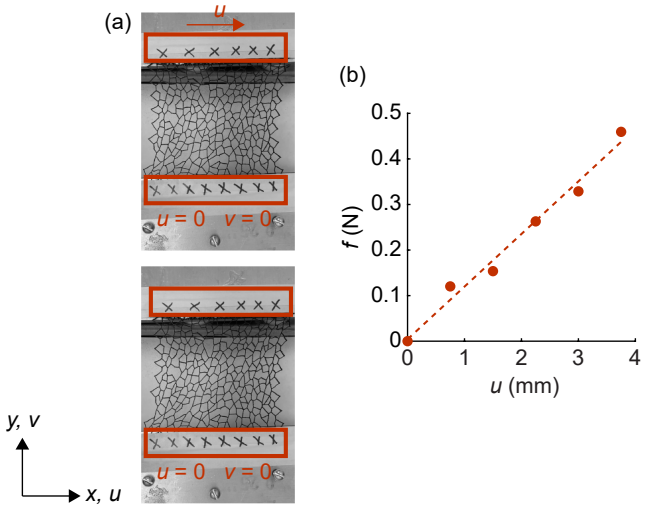

Figure 8: Simple shear test on the fabricated specimen at zero pretension. (a) The specimen was subjected to simple shear by displacing the top edge by u in the positive x direction while constraining the bottom edge. The top and bottom edges are highlighted by red boundaries. The top frame shows the reference configuration and the bottom frame shows the deformed configuration. (b) The shear force responses (f) in the specimen were plotted against the corresponding shear displacements (u). The dashed line represents a linear best fit.

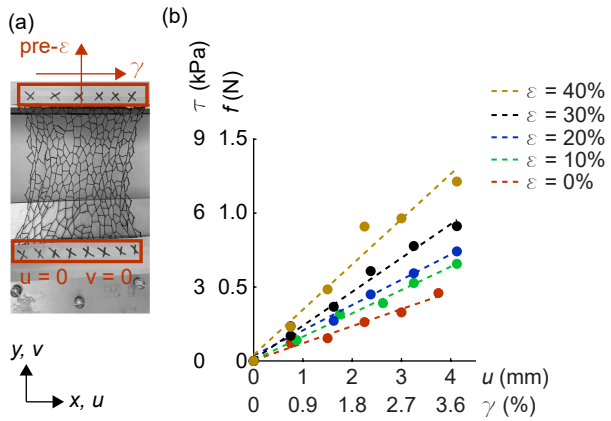

Figure 9: Simple shear test on the fabricated specimen at varying levels of pretension. (a) Representative image showing the specimen subjected to a pretension $\varepsilon = 30\%$ and shear strain $\gamma = 3.6\%$. The top and bottom grips are highlighted by red boxes. (b) The force–displacement (f & u) and the stress–strain (τ & γ) responses in shear at different pretensions in the specimen. The values of small strain shear stiffness (G_0) as indicated by the slopes of the best-fit linear τ–γ responses (dashed lines) were 77.0, 105, 114, 153 and 204 kPa for, respectively, pretensions of $\varepsilon = 0$, 10, 20, 30 and 40%. This observed increase in shear stiffness with increasing pretension indicates prestrain-induced stiffening in the fabricated network.

Comparing Experimental Results with Simulations

We compared the values of small strain shear stiffness (G_0) of the fabricated network at different pretensions with the corresponding finite element results (Fig. 10). Firstly, we compared the experimental results with the simulations on the simplified network model where fibers exhibited linear material response (Fig. 10a). In the absence of pretension ($\varepsilon = 0$), the stiffness obtained from the experiment (77.0 kPa) matched closely with the simulation (82.2 kPa), but at finite pretensions ($\varepsilon > 0$), the fabricated network exhibited far less stiffening than the prediction in the simulations.

Next, we compared the experimental results with the simulations performed on the updated network model wherein the fibers possessed the nonlinear material response of the printing resin (Fig. 10b). Interestingly, the stiffness obtained from these simulations matched closely with the experiments, both in the absence and presence of finite pretensions. For example, the values of shear stiffness predicted by the simulations deviated only by 6.8% and 5.9% at pretensions of $\varepsilon = 0$ and $\varepsilon = 40\%$, respectively. Even though the resin itself softened, the stiffening caused by the geometric nonlinearity had a larger effect, thereby producing stiffening of the overall network.

Conclusions and Outlook

Here we developed a new workflow to generate STL files of fiber networks for additive manufacturing. This method can generate aperiodic, random fiber networks whose morphological disorder can be tuned to match the micro-architectures of biopolymer networks. To demonstrate the technique, we fabricated one representative network using DLP technology in a commercial 3D printer. Both simulations and experiments demonstrated the presence of tunability of shear stiffness, with shear stiffness increasing with increasing pretension. Strain softening of the printed resin partially, but not fully, reduced the amount of pretension-induced stiffening observed.

The workflow to generate STL files described in this manuscript is general in the sense that the fibers can be arranged to form networks of any architecture, having desired distributions of fiber lengths, connections, and alignment. Moreover, this workflow is also applicable for a network of fibers organized in a 3D domain.

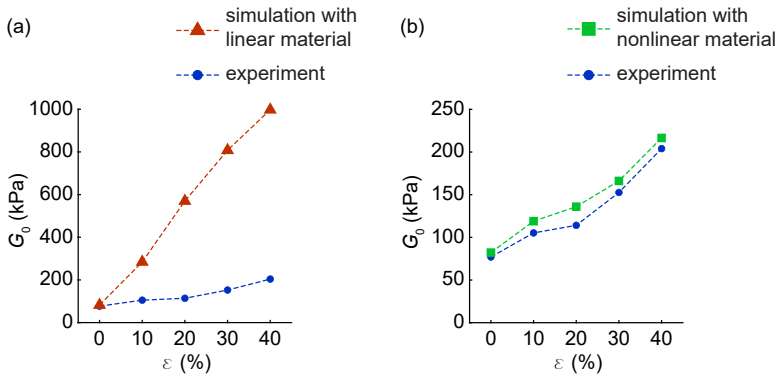

Figure 10: Comparison between the finite element simulations and experimental results, depicting the dependence of the small strain shear stiffness (G_0) on the pretension (ε) for both the numerical model and the fabricated specimen. (a) The experimental results and predictions from simulations with the linear material. (b) The experimental results and predictions from simulations with the nonlinear material (EPU 40). Consideration of the strain softening response of the fibers in the simulations resulted in the close agreement between simulation predictions and experiments.

Fabrication of a 3D network, however, remains challenging, because 3D disordered networks are not self-supporting, meaning that the out-of-plane fibers do not support the in-plane fibers during fabrication, which requires additional supporting scaffolds. The support materials used in commercial DLP fabrication are made of constituents similar to that of the specimen to be manufactured, and manual removal of these supports remains a challenge, meaning that the use of commercial DLP is restricted to 2D networks. This challenge could likely be addressed by complementing conventional DLP with multi-material projection lithography [70], wherein a second resin is used to make chemically dissolvable supports. Therefore, with systematic integration of recent developments in downstream fabrication, and incorporating our workflow to address the existing challenges in upstream modeling, we anticipate that, in the near future, it will be possible to design bioinspired fiber networks for applications requiring controllable mechanical properties.

Acknowledgments

This work was supported by the National Science Foundation grant number CMMI-1749400.

Declarations

Conflicts of Interest

The authors have no conflicts of interest to declare.

Code Availability

The code for making the fiber networks is available from https://github.com/jknotbohm/fiber_network_model. The code for making STL files of fiber networks for additive manufacturing is available from https://github.com/jknotbohm/stl_generation. There exist options to generate STL files from both two- and three-dimensional models of networks.

Appendix A: Convergence of the Explicit Dynamic Solver

To verify that the explicit dynamic solver converged correctly, we ensured that the model remained slightly underdamped for all simulations. To this end, we studied the time evolution of the model kinetic energy (Fig. 11a). The presence of few initial oscillations in the kinetic energy (for time steps < 500, Fig. 11a) prior to steady state indicated that the solver was not overdamped. The total time step considered in the

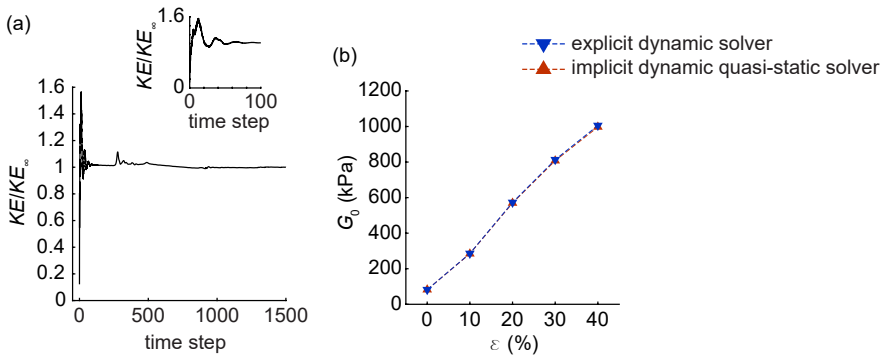

Figure 11: Convergence of the explicit dynamic solver. (a) The evolution of the model kinetic energy (KE) with simulation time step. The kinetic energy was normalized with its steady state value (KE_∞). The inset shows the initial oscillations of the kinetic energy up to the time step of 100. The presence of a few initial oscillations of the KE ensured that the model was slightly underdamped. (b) Comparison of results for shear stiffness between the explicit dynamic solver and the implicit dynamic quasi-static solver. Simulations were performed on the model of the network with fibers exhibiting linear material response. At all pretensions ($\varepsilon = 0, 10, 20, 30, 40\%$), the predictions of the values of small strain shear stiffness by the explicit dynamic solver matched closely with the corresponding predictions of the implicit dynamic quasi-static solver.

analysis was sufficient to ensure that the model kinetic energy fell below 0.001% of the model strain energy.

Next, we verified the results of the explicit dynamic solver against the implicit quasi-static solver. To this end, we considered the simplified model of the fiber network where fibers possessed linear stress–strain response. Pretension and shear were applied to the fiber network model, and the model was solved using both solvers. The values of small strain shear stiffness predicted by the explicit dynamic solver at all pretensions closely matched the corresponding predictions of the implicit dynamic quasi-static solver (Fig. 11b), indicating correct convergence of the explicit dynamic solver.

Appendix B: Effect of Boundaries

Both rigidity and proximity of boundaries can alter the mechanical response of fiber networks [61, 63, 69]. The experiments used a printed square network that was glued to the plates of the test device before applying tension, meaning that the nodes at the boundaries of the specimen were constrained along both the x and y directions, and the simulations reported in the main text matched these conditions. The choice of using a square specimen combined with constraining displacements in the x direction creates a boundary effect, and, in principle, it could be possible to reduce or eliminate the boundary effect by using a specimen with an aspect ratio > 1. To investigate whether a specimen of large aspect ratio would exhibit a reduced boundary effect, we performed additional simulations with and without constraining the lateral (x) component of displacement of the boundary nodes (Fig. 12a, b). The values of small strain shear stiffness of the pretensioned model with and without the lateral constraint, G_1 and G_2, respectively, were compared to quantify the effect of the boundaries. For the square specimen (height-to-width ratio $H/W = 1$) the ratio G_1/G_2 was 1.65 at the highest pretension of $\varepsilon = 40\%$ (Fig. 12c). We next studied models of networks with varying height-to-width ratios H/W (Fig. 12c). At $\varepsilon = 40\%$, the ratio G_1/G_2 decreased slowly, starting from a value of 1.65 at $H/W = 1$ and decreasing to 1.34 at $H/W = 6$. These results suggested that the effect of boundaries was unavoidable for all practically feasible dimensions of the fiber network.

References

[1] Sanchez, C., Arribart, H., and Giraud Guille, M. M., 2005. "Biomimetism and bioinspiration as tools for the design of innovative materials and systems". *Nat Mater,* **4**(4), pp. 277–288.

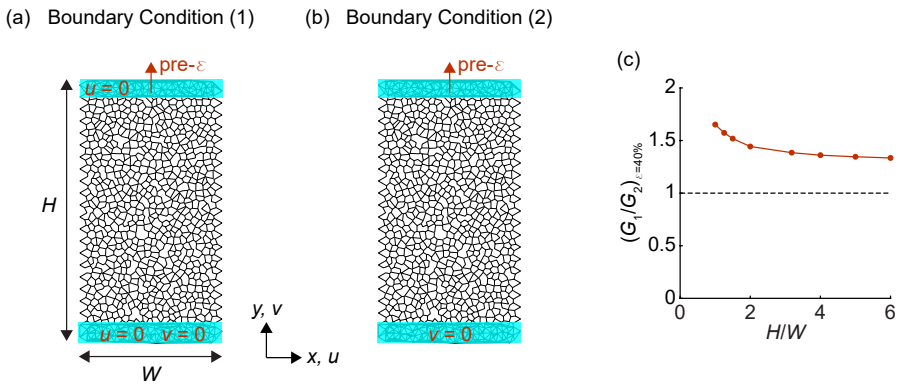

Figure 12: Quantifying the boundary effect in the fiber network. (a) The first boundary condition matching the experimental situation. During pretension (ε), the lateral (x directional) movement of the boundary nodes (shaded blue) was constrained. The height and width of the network are H and W respectively. The small strain shear stiffness of the pretensioned network subjected to boundary condition (1) was defined as G_1. (b) The second boundary condition, wherein boundary nodes (shaded blue) were freely allowed to move in the lateral direction (x direction) during pretension (ε). The small strain shear stiffness of the pretensioned network subjected to boundary condition (2) was defined as G_2. (c) The values of small strain shear stiffness of the pretensioned network from boundary conditions (1) and (2) were compared to quantify the boundary effect. At the highest pretension ($\varepsilon = 40\%$), the ratios G_1/G_2 were calculated for different networks with varying height-to-width ratios (H/W). The dashed line at $G_1/G_2 = 1$ corresponds to the absence of boundary effect.

[2] Janmey, P. A., 1998. "The cytoskeleton and cell signaling: component localization and mechanical coupling". *Physiol Rev,* **78**(3), pp. 763–781.

[3] Bausch, A., and Kroy, K., 2006. "A bottom-up approach to cell mechanics". *Nat Phys,* **2**(4), pp. 231–238.

[4] Alberts, B., Johnson, A., Lewis, J., Raff, M., Roberts, K., and Walter, P., 2007. *Molecular Biology of the Cell*. Taylor & Francis Group, New York.

[5] Muiznieks, L. D., and Keeley, F. W., 2013. "Molecular assembly and mechanical properties of the extracellular matrix: A fibrous protein perspective". *BBA-Mol Basis Dis,* **1832**(7), pp. 866–875.

[6] Laurens, N., Koolwijk, P. d., and De Maat, M., 2006. "Fibrin structure and wound healing". *J Thromb Haemost,* **4**(5), pp. 932–939.

[7] Licup, A. J., Münster, S., Sharma, A., Sheinman, M., Jawerth, L. M., Fabry, B., Weitz, D. A., and MacKintosh, F. C., 2015. "Stress controls the mechanics of collagen networks". *P Natl Acad Sci USA,* **112**(31), pp. 9573–9578.

[8] Vahabi, M., Sharma, A., Licup, A. J., Van Oosten, A. S., Galie, P. A., Janmey, P. A., and MacKintosh, F. C., 2016. "Elasticity of fibrous networks under uniaxial prestress". *Soft matter,* **12**(22), pp. 5050–5060.

[9] Picu, R., Deogekar, S., and Islam, M., 2018. "Poisson's contraction and fiber kinematics in tissue: insight from collagen network simulations". *J Biomech Eng-T ASME,* **140**(2), p. 021002.

[10] Liang, L., Jones, C., Chen, S., Sun, B., and Jiao, Y., 2016. "Heterogeneous force network in 3d cellularized collagen networks". *Phys Biol,* **13**(6), p. 066001.

[11] Ronceray, P., Broedersz, C. P., and Lenz, M., 2016. "Fiber networks amplify active stress". *P Natl Acad Sci USA,* **113**(11), pp. 2827–2832.

[12] Burkel, B., and Notbohm, J., 2017. "Mechanical response of collagen networks to nonuniform microscale loads". *Soft Matter,* **13**(34), pp. 5749–5758.

[13] Grimmer, P., and Notbohm, J., 2018. "Displacement propagation in fibrous networks due to local contraction". *J Biomech Eng—T ASME,* **140**(4), p. 041011.

[14] Roeder, B. A., Kokini, K., Sturgis, J. E., Robinson, J. P., and Voytik-Harbin, S. L., 2002. "Tensile mechanical properties of three-dimensional type i collagen extracellular matrices with varied microstructure". *J Biomech Eng-T ASME,* **124**(2), pp. 214–222.

[15] Janmey, P. A., McCormick, M. E., Rammensee, S., Leight, J. L., Georges, P. C., and MacKintosh, F. C., 2007. "Negative normal stress in semiflexible biopolymer gels". *Nat Mater,* **6**(1), pp. 48–51.

[16] Brown, A. E., Litvinov, R. I., Discher, D. E., Purohit, P. K., and Weisel, J. W., 2009. "Multiscale mechanics of fibrin polymer: gel stretching with protein unfolding and loss of water". *Science,* **325**(5941), pp. 741–744.

[17] Vader, D., Kabla, A., Weitz, D., and Mahadevan, L., 2009. "Strain-induced alignment in collagen gels". *Plos One,* **4**(6), p. e5902.

[18] Münster, S., Jawerth, L. M., Leslie, B. A., Weitz, J. I., Fabry, B., and Weitz, D. A., 2013. "Strain history dependence of the nonlinear stress response of fibrin and collagen networks". *P Natl Acad Sci USA,* **110**(30), pp. 12197–12202.

[19] Kim, O. V., Litvinov, R. I., Weisel, J. W., and Alber, M. S., 2014. "Structural basis for the nonlinear mechanics of fibrin networks under compression". *Biomaterials,* **35**(25), pp. 6739–6749.

[20] Jen, C. J., and McIntire, L. V., 1982. "The structural properties and contractile force of a clot". *Cell Motil Cytoskel,* **2**(5), pp. 445–455.

[21] Taylor, C. A., and Humphrey, J., 2009. "Open problems in computational vascular biomechanics: hemodynamics and arterial wall mechanics". *Comput Method Appl M,* **198**(45-46), pp. 3514–3523.

[22] Ingber, D. E., 2006. "Cellular mechanotransduction: putting all the pieces together again". *FASEB J,* **20**(7), pp. 811–827.

[23] Destrade, M., Liu, Y., Murphy, J. G., and Kassab, G. S., 2012. "Uniform transmural strain in prestressed arteries occurs at physiological pressure". *J Theor Biol,* **303**, pp. 93–97.

[24] Van Oosten, A. S., Vahabi, M., Licup, A. J., Sharma, A., Galie, P. A., MacKintosh, F. C., and Janmey, P. A., 2016. "Uncoupling shear and uniaxial elastic moduli of semiflexible biopolymer networks: compression-softening and stretch-stiffening". *Sci Rep,* **6**, p. 19270.

[25] Ban, E., Wang, H., Franklin, J. M., Liphardt, J. T., Janmey, P. A., and Shenoy, V. B., 2019. "Strong triaxial coupling and anomalous poisson effect in collagen networks". *P Natl Acad Sci USA,* **116**(14), pp. 6790–6799.

[26] Hatami-Marbini, H., and Rohanifar, M., 2021. "Nonlinear mechanical properties of prestressed branched fibrous networks". *Biophys J,* **120**(3), pp. 527–538.

[27] Koh, C., and Oyen, M., 2012. "Branching toughens fibrous networks". *J Mech Behav Biomed,* **12**, pp. 74–82.

[28] Storm, C., Pastore, J. J., MacKintosh, F. C., Lubensky, T. C., and Janmey, P. A., 2005. "Nonlinear elasticity in biological gels". *Nature,* **435**(7039), pp. 191–194.

[29] Jang, K.-I., Chung, H. U., Xu, S., Lee, C. H., Luan, H., Jeong, J., Cheng, H., Kim, G.-T., Han, S. Y., Lee, J. W., et al., 2015. "Soft network composite materials with deterministic and bio-inspired designs". *Nat Commun,* **6**, p. 6566.

[30] Jiang, Y., and Wang, Q., 2016. "Highly-stretchable 3d-architected mechanical metamaterials". *Sci Rep-UK,* **6**, p. 34147.

[31] Yan, D., Chang, J., Zhang, H., Liu, J., Song, H., Xue, Z., Zhang, F., and Zhang, Y., 2020. "Soft three-dimensional network materials with rational bio-mimetic designs". *Nat Commun,* **11**, p. 1180.

[32] Lee, P., Lee, J., Lee, H., Yeo, J., Hong, S., Nam, K. H., Lee, D., Lee, S. S., and Ko, S. H., 2012. "Highly stretchable and highly conductive metal electrode by very long metal nanowire percolation network". *Adv Mater,* **24**(25), pp. 3326–3332.

[33] Wu, H., Chan, G., Choi, J. W., Ryu, I., Yao, Y., McDowell, M. T., Lee, S. W., Jackson, A., Yang, Y., Hu, L., et al., 2012. "Stable cycling of double-walled silicon nanotube battery anodes through solid–electrolyte interphase control". *Nat Nanotechnol,* **7**(5), pp. 310–315.

[34] Yu, C., Masarapu, C., Rong, J., Wei, B., and Jiang, H., 2009. "Stretchable supercapacitors based on buckled single-walled carbon-nanotube macrofilms". *Adv Mater,* **21**(47), pp. 4793–4797.

[35] Kinstlinger, I. S., Bastian, A., Paulsen, S. J., Hwang, D. H., Ta, A. H., Yalacki, D. R., Schmidt, T., and Miller, J. S., 2016. "Open-source selective laser sintering (opensls) of nylon and biocompatible polycaprolactone". *PloS One,* **11**(2), p. e0147399.

[36] Zheng, X., Deotte, J., Alonso, M. P., Farquar, G. R., Weisgraber, T. H., Gemberling, S., Lee, H., Fang, N., and Spadaccini, C. M., 2012. "Design and optimization of a light-emitting diode projection micro-stereolithography three-dimensional manufacturing system". *Rev Sci Instrum,* **83**(12), p. 125001.

[37] Yeong, W., Sudarmadji, N., Yu, H., Chua, C., Leong, K., Venkatraman, S., Boey, Y., and Tan, L., 2010. "Porous polycaprolactone scaffold for cardiac tissue engineering fabricated by selective laser sintering". *Acta Biomater,* **6**(6), pp. 2028–2034.

[38] Xue, D., Zhang, J., Wang, Y., and Mei, D., 2019. "Digital light processing-based 3d printing of cell-seeding hydrogel scaffolds with regionally varied stiffness". *ACS Biomater Sci Eng,* **5**(9), pp. 4825–4833.

[39] Teng, C.-L., Chen, J.-Y., Chang, T.-L., Hsiao, S.-K., Hsieh, Y.-K., Gorday, K. V., Cheng, Y.-L., and Wang, J., 2020. "Design of photocurable, biodegradable scaffolds for liver lobule regeneration via digital light process-additive manufacturing". *Biofabrication,* **12**(3), p. 035024.

[40] Rens, R., 2019. "Theory of rigidity transitions in disordered materials". PhD thesis, University of Amsterdam.

[41] Nguyen, D. S., 2019. "A method for generation of random lattice structure for additive manufacturing". In 2019 IEEE International Conference on Industrial Engineering and Engineering Management (IEEM), IEEE, pp. 1275–1279.

[42] Cai, L., Li, J., Luan, P., Dong, H., Zhao, D., Zhang, Q., Zhang, X., Tu, M., Zeng, Q., Zhou, W., et al., 2012. "Highly transparent and conductive stretchable conductors based on hierarchical reticulate single-walled carbon nanotube architecture". *Adv Funct Mater,* **22**(24), pp. 5238–5244.

[43] Lu, W., Sun, J., and Jiang, X., 2014. "Recent advances in electrospinning technology and biomedical applications of electrospun fibers". *J Mater Chem B,* **2**(17), pp. 2369–2380.

[44] Xu, F., and Zhu, Y., 2012. "Highly conductive and stretchable silver nanowire conductors". *Adv Mater,* **24**(37), pp. 5117–5122.

[45] Islam, M., and Picu, R., 2018. "Effect of network architecture on the mechanical behavior of random fiber networks". *J Appl Mech,* **85**(8), p. 081011.

[46] Arzash, S., Shivers, J. L., Licup, A. J., Sharma, A., and MacKintosh, F. C., 2019. "Stress-stabilized subisostatic fiber networks in a ropelike limit". *Phys Rev E,* **99**(4), p. 042412.

[47] Heussinger, C., and Frey, E., 2006. "Stiff polymers, foams, and fiber networks". *Phys Rev Lett,* **96**(1), p. 017802.

[48] Kumar, S., and Kurtz, S. K., 1993. "Properties of a two-dimensional poisson-voronoi tesselation: a monte-carlo study". *Mater Charact,* **31**(1), pp. 55–68.

[49] Maxwell, J. C., 1864. "L. on the calculation of the equilibrium and stiffness of frames". *Lond Edinb Dublin Philos Mag J Sci,* **27**(182), pp. 294–299.

[50] Heussinger, C., and Frey, E., 2007. "Force distributions and force chains in random stiff fiber networks". *Eur Phys J E,* **24**(1), pp. 47–53.

[51] Picu, R., 2011. "Mechanics of random fiber networks—a review". *Soft Matter,* **7**(15), pp. 6768–6785.

[52] Head, D. A., Levine, A. J., and MacKintosh, F., 2003. "Deformation of cross-linked semiflexible polymer networks". *Phys Rev Lett,* **91**(10), p. 108102.

[53] Wilhelm, J., and Frey, E., 2003. "Elasticity of stiff polymer networks". *Phys Rev Lett,* **91**(10), p. 108103.

[54] Feng, J., Levine, H., Mao, X., and Sander, L. M., 2015. "Alignment and nonlinear elasticity in biopolymer gels". *Phys Rev E,* **91**(4), p. 042710.

[55] Chen, Z., Li, Z., Li, J., Liu, C., Lao, C., Fu, Y., Liu, C., Li, Y., Wang, P., and He, Y., 2019. "3d printing of ceramics: A review". *J Eur Ceram Soc,* **39**(4), pp. 661–687.

[56] Sun, C., Fang, N., Wu, D., and Zhang, X., 2005. "Projection micro-stereolithography using digital micro-mirror dynamic mask". *Sensor Actuat A-Phys,* **121**(1), pp. 113–120.

[57] Montemayor, L. C., Meza, L. R., and Greer, J. R., 2014. "Design and fabrication of hollow rigid nanolattices via two-p hoton lithography". *Adv Eng Mater,* **16**(2), pp. 184–189.

[58] Shuai, X., Zeng, Y., Li, P., and Chen, J., 2020. "Fabrication of fine and complex lattice structure al2o3 ceramic by digital light processing 3d printing technology". *J Mater Sci,* **55**(16), pp. 6771–6782.

[59] Graziosi, S., Ballo, F. M., Libonati, F., and Senna, S., 2022. "3d printing of bending-dominated soft lattices: numerical and experimental assessment". *Rapid Prototyping J,* **28**(11), pp. 51–64.

[60] Aguirre, T. G., Fuller, L., Ingrole, A., Seek, T. W., Wheatley, B. B., Steineman, B. D., Donahue, T. L. H., and Donahue, S. W., 2020. "Bioinspired material architectures from bighorn sheep horncore velar bone for impact loading applications". *Sci Rep,* **10**, p. 18916.

[61] Shahsavari, A., and Picu, R., 2013. "Size effect on mechanical behavior of random fiber networks". *Int J Solids Struct,* **50**(20-21), pp. 3332–3338.

[62] Shahsavari, A., and Picu, R., 2012. "Model selection for athermal cross-linked fiber networks". *Phys Rev E,* **86**(1), p. 011923.

[63] Tyznik, S., and Notbohm, J., 2019. "Length scale dependent elasticity in random three-dimensional fiber networks". *Mech Mater,* **138**, p. 103155.

[64] Sarkar, M., and Notbohm, J., 2022. "Evolution of force chains explains the onset of strain stiffening in fiber networks". *J Appl Mech,* **89**(11), p. 111008.

[65] Proestaki, M., Burkel, B., Galles, E. E., Ponik, S. M., and Notbohm, J., 2021. "Effect of matrix heterogeneity on cell mechanosensing". *Soft Matter,* **17**, pp. 10263–10273.

[66] Sarkar, M., and Notbohm, J., 2022. "Quantification of errors in applying dic to fiber networks imaged by confocal microscopy". *Exp Mech,* **62**(7), pp. 1175–1189.

[67] International, A., 2005. *ASTM D 7078, Standard Test Method for Shear Properties of Composite Materials by V-notched Rail Shear Method*. West Conshohocken, PA.

[68] Adams, D. O., Moriarty, J. M., Gallegos, A. M., and Adams, D. F., 2007. "The v-notched rail shear test". *J Compos Mater,* **41**(3), pp. 281–297.

[69] Merson, J., and Picu, R., 2020. "Size effects in random fiber networks controlled by the use of generalized boundary conditions". *Int J Solids Struct,* **206**, pp. 314–321.

[70] Xu, Z., Hensleigh, R., Gerard, N. J., Cui, H., Oudich, M., Chen, W., Jing, Y., and Zheng, X. R., 2021. "Vat photopolymerization of fly-like, complex micro-architectures with dissolvable supports". *Addit Manuf,* **47**, p. 102321.